Holographic simulation of correlated electrons on a trapped ion quantum processor

Daoheng Niu,[1,*] Reza Haghshenas,[2,†] Yuxuan Zhang,[1] Michael Foss-Feig,[3] Garnet Kin-Lic Chan,[2] and Andrew C. Potter[4]

[1] *Department of Physics, University of Texas at Austin, Austin, TX 78712, USA*
[2] *Division of Chemistry and Chemical Engineering, California Institute of Technology, Pasadena, California 91125, USA*
[3] *Quantinuum, 303 S Technology Ct. Broomfield, CO, 80021, USA*
[4] *Department of Physics and Astronomy, and Stewart Blusson Quantum Matter Institute, University of British Columbia, Vancouver, BC, Canada V6T 1Z1*

We develop holographic quantum simulation techniques to prepare correlated electronic ground states in quantum matrix product state (qMPS) form, using far fewer qubits than the number of orbitals represented. Our approach starts with a holographic technique to prepare a compressed approximation to electronic mean-field ground-states, known as fermionic Gaussian matrix product states (GMPS), with a polynomial reduction in qubit- and (in select cases gate-) resources compared to existing techniques. Correlations are then introduced by augmenting the GMPS circuits in a variational technique which we denote GMPS+U. We demonstrate this approach on Quantinuum's System Model H1 trapped-ion quantum processor for $1d$ models of correlated metal and Mott insulating states. Focusing on the $1d$ Fermi-Hubbard chain as a benchmark, we show that GMPS+U methods faithfully capture the physics of correlated electron states, including Mott insulators and correlated Luttinger liquid metals, using considerably fewer parameters than problem-agnostic variational circuits.

Introduction – As quantum computers have begun to achieve scale and reliability required to surpass classical computations on certain theoretically-contrived tasks such as random quantum circuit sampling [1–3], it is natural to ask how best to apply their computational abilities to problems of technological and scientific interest. The quantum simulation of molecules and materials is a promising target application, where there are theoretical grounds to expect exponential quantum computational advantage [4] in certain types of quantum dynamics, with prospective applications to non-equilibrium electron transport, quantum reactive scattering, and the dynamics of strongly-coupled field theories. An important prerequisite to computing dynamics in physical applications is to first prepare a good approximation to the ground- or thermal-state of a correlated electron system. In variational approaches, a key goal is to use physically-inspired circuit ansatzes to reduce the number of variational parameters and simplify the optimization landscape. Matrix-product states (MPS) [5] provide a compact parameterization of many physically-important quantum states, since the memory and complexity of MPS calculations is controlled by the extent of spatial correlations and entanglement, encoded by the matrix size ("bond-dimension") χ. A growing body of work [6–12] has begun to extend the efficient data compression afforded by classical MPS techniques to the quantum domain, using quantum memories with $\sim \log_2 \chi$ qubits to represent the bond-space of an MPS, and quantum circuits interleaved with partial-measurement to implement its tensors. By exploiting mid-circuit measurements and qubit reuse (MCMR) [7], a quantum MPS (qMPS) simulation of a d-dimensional systems can be performed with effectively $(d-1)$ dimensions' worth of qubits, earning the moniker "holographic simulation" [7, 13]. Early demonstrations of holographic qMPS [6, 7, 9] and their higher-dimensional quantum tensor network (qTNS) generalizations [11, 12] have focused on simple spin models. However, more realistic molecular and material models contain fermionic electrons, which commonly exhibit quite entangled (e.g. metallic) ground-states even for weak interaction strengths, and whose Hamiltonians have more complex qubit representations.

Because many correlated electron states are adiabatically connected to Gaussian (e.g. mean-field) states, we first describe how to prepare holographically Gaussian MPS (GMPS) as a qMPS. We start from a classical construction of Fishman and White [14] that naturally compresses Gaussian fermionic states in GMPS form. A key aspect to this compression is that, unlike other mean-field preparation techniques, it exploits the near-area-law nature of the ground-state to parametrically reduce qubit and gate resources. We present numerical evidence that this holographic GMPS method gives a polynomial reduction in the number of qubits (and in certain cases, gates) compared to standard quantum algorithms. Next, using the $1d$ Fermi-Hubbard chain as a benchmark, we show that augmenting the mean-field GMPS state with shallow circuits (a method we refer to as GMPS+U) enables the variational preparation of correlated electron ground-states with far-fewer parameters than problem-agnostic ansatzes, a key component for scaling up qMPS methods to solve larger and more classically-challenging models. We implement the GMPS and GMPS+U methods on Quantinuum's system model H1 trapped-ion quantum processor, demonstrating that

* daoheng@utexas.edu
† haqshena@caltech.edu

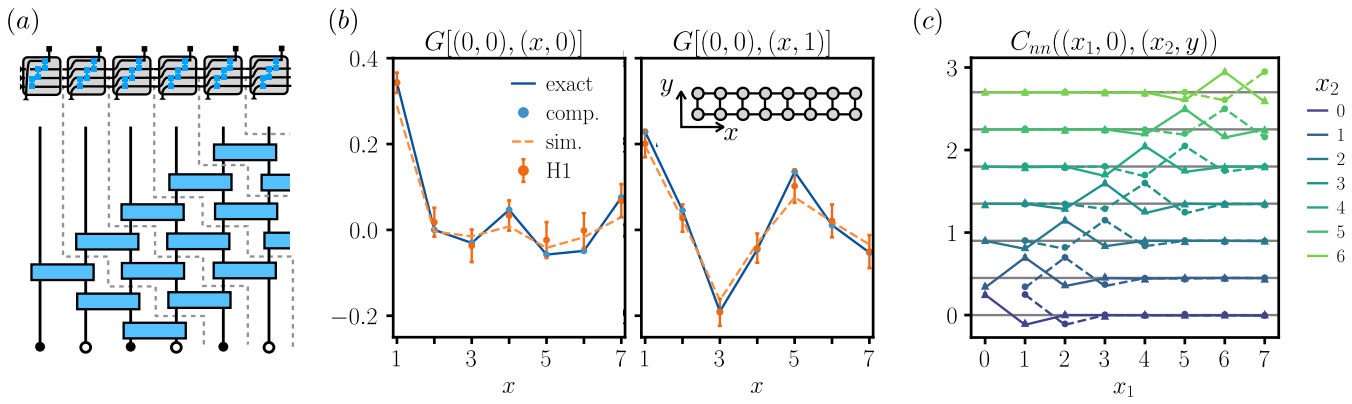

FIG. 1. **Compressing Gaussian Fermion States as qMPS** – (a) Holographic qMPS implementation (top) of the GMPS circuit (bottom) for approximately preparing compressed Gaussian fermion states. (b-c) Experimental implementation of holographic GMPS algorithm for a spinless two-leg ladder at half-filling. (b) (Real-part of) Green's function, $\Re\mathrm{e}\, G\left[\boldsymbol{r}=0,\boldsymbol{r}'=(x,y)\right]$ with experimental data (orange dots with 1σ error bars from 1000 measurement shots per point), noisy circuit simulations with one-qubit and two-qubit gate depolarizing parameters $p_{1q}=10^{-3}$ and $p_{2q}=5\cdot10^{-3}$ respectively (dashed orange line), and exact values (solid blue line)). (c) Connected part of density-density correlators $C_{nn}(\boldsymbol{r},\boldsymbol{r}')$ with $\boldsymbol{r}=(x_1,0)$ and $\boldsymbol{r}'=(x_2,y)$, with $y=0$ data shown as solid-lines (theory) and triangles (experiment), and $y=1$ data shown as dashed-lines (theory) and circles (experiment) respectively. Each point represents 5600 measurement shots. Statistical error bars in (c) are included, but smaller than plot symbols.

the resource reductions enable the faithful simulation of systems with up to 16 orbitals using minimal error mitigation.

Quantum Matrix Product States (qMPS) – Holographic simulation with qMPS is based on the matrix-product state (MPS) representation:

$$|\Psi\rangle=\sum_{n_1\ldots n_L}\ell^T A^{n_1}A^{n_2}\ldots|n_1n_2\ldots n_L\rangle \tag{1}$$

where $n_x\in\{1,2,\ldots d=2^{N_p}\}$ label the orbital occupation numbers of the N_p different physical spin- or orbital-"flavors" at position x, A^{n_x} is a $\chi\times\chi$ matrix for each n_x label, and ℓ is a χ-dimensional vector that determines the left boundary-conditions. $2d$ and $3d$ systems can also be treated in this framework by treating the system as a $1d$ stack of $(d-1)$-dimensional cross-sections. In this case, χ must scale exponentially in the cross-sectional area for area-law states.

Properties of any MPS in right-canonical form (RCF) [15] can be measured on a quantum computer by implementing its transfer-matrix as a quantum channel [16] acting on $N_p=\log_2 d$ "physical" qubits and $N_b=\log_2\chi$ bond qubits. The bond-vector ℓ is prepared by acting on the bond-qubits plus optional ancilla with a unitary U_ℓ. Each tensor A is then embedded into a larger block unitary operator U_A acting on a reference initial state, $|0\rangle$, of the physical qubits: $A^n_{ij}=\langle n|_p\otimes\langle i|_b U_A|0\rangle_p\otimes|j\rangle_b$ where subscripts p and b respectively denote physical and bond qubits. Then, the physical qubits can be measured in any desired basis (without measuring the bond qubits). The process is then repeated for each site in sequence from left to right until the measurement is completed. As for any quantum algorithm, repeated statistical sampling of these measurements must be used to estimate expectation values of observables. In this way, one can measure any product operator of the form $\prod_{x=1}^{L}\mathcal{O}_x$, which form a complete basis for general observables. Moreover, the entanglement spectrum of the bond-qubits in between sites x and $x+1$ coincides with the bipartite entanglement spectrum of the physical MPS at that entanglement cut, further enabling measurement of non-local entanglement observables, as recently demonstrated experimentally for near-critical spin chains [7].

Models and Observables – We focus on quasi-1d Fermi-Hubbard (FH) models, which we write in the form:

$$H_{\mathrm{FH}}=-t\sum_{\sigma,\langle\boldsymbol{r},\boldsymbol{r}'\rangle}c^\dagger_{\boldsymbol{r},\sigma}c_{\boldsymbol{r}',\sigma}+\frac{U}{2}\sum_{\boldsymbol{r}}n_{\boldsymbol{r}}\left(n_{\boldsymbol{r}}-1\right)-\mu N \tag{2}$$

where $c^\dagger_{\boldsymbol{r},\sigma}$ creates an electron at site $\boldsymbol{r}=(x,y)$ with z-component of spin $\sigma\in\{\uparrow,\downarrow\}$, $1\le x,y\le L_{x,y}$, $n_{\boldsymbol{r}}=\sum_\sigma c^\dagger_{\boldsymbol{r}\sigma}c_{\boldsymbol{r}\sigma}$, $N=\sum_{\boldsymbol{r}}n_{\boldsymbol{r}}$, t is the hopping strength, U is the onsite Hubbard interaction, and μ is the chemical potential. We measure two types of observables, single-particle, equal-time Green's functions (one-electron density matrices) $G_{\boldsymbol{r},\sigma;\boldsymbol{r}',\sigma'}=\langle c^\dagger_{\boldsymbol{r},\sigma}c_{\boldsymbol{r}',\sigma'}\rangle$, and connected density-density and spin-spin correlators $C_{nn}(\boldsymbol{r},\boldsymbol{r}')=\langle n_{\boldsymbol{r}}n_{\boldsymbol{r}'}\rangle-\langle n_{\boldsymbol{r}}\rangle\langle n_{\boldsymbol{r}'}\rangle$, $C_{SS}(\boldsymbol{r},\boldsymbol{r}')=\langle S^z_{\boldsymbol{r}}S^z_{\boldsymbol{r}'}\rangle-\langle S^z_{\boldsymbol{r}}\rangle\langle S^z_{\boldsymbol{r}'}\rangle$ (where $S^z_{\boldsymbol{r}}=\frac{1}{2}\sum_{\sigma,\sigma'}c^\dagger_{\boldsymbol{r},\sigma}\sigma^z_{\sigma\sigma'}c_{\boldsymbol{r},\sigma'}$) .

To simulate fermionic systems, one needs to encode the physical fermionic orbital creation and annihilation operators into bosonic qubit degrees of freedom. A variety of encodings are available. Throughout this work, we adopt the Jordan-Wigner (JW) encoding, which is

natural for quasi-1d settings, with the convention that orbitals are ordered first by spin $\{\uparrow,\downarrow\}$, then by ascending y-position, and finally by ascending x-position. We remark that the holographic representation in principle enables (Appendix F) one to reduce the maximal length of JW strings that one needs to measure in variational calculations from $\sim L^d \to L^{d-1}$, reducing the impact of measurement-errors in computing long-distance correlation functions.

Compressing Gaussian States as qMPS – We begin by briefly reviewing the classical MPS algorithm to construct an MPS representation of Gaussian fermion states, and explain how to recast the resulting Gaussian MPS (GMPS) as a qMPS. The ground-state of a non-interacting fermion Hamiltonian with N_o orbitals: $H = \sum_{i,j=1}^{N_\mathrm{o}} c_i^\dagger h_{ij} c_j$ is fully characterized by its $N_\mathrm{o} \times N_\mathrm{o}$ single particle Green's function: $G_{ij} = \langle c_i^\dagger c_j \rangle$ (generalizations to non-number conserving Hamiltonians are discussed in Appendix E), which has highly-degenerate eigenvalues of either 0 or 1 and whose eigenvectors correspond to unoccupied or occupied orbitals respectively. The Green's function is preserved by any unitary transformation acting separately on the (un)occupied subspaces. The compression scheme of [14] exploits this freedom by progressively disentangling well-localized degrees of freedom in blocks of B adjacent sites, where B is chosen to be sufficiently large to achieve target infidelity, ϵ. Starting with the upper-left $B \times B$ block of G, one finds the eigenvector of this sub-block whose eigenvalue is closest to either 0 or 1, and performs a series of 2×2 (single-particle) unitary rotations that move this eigenvector to the first site of the block. The procedure is iterated for the remaining $(N_\mathrm{o} - 1) \times (N_\mathrm{o} - 1)$ sites until the Green's function is approximately diagonalized.

The composition of all the basis rotations in the above procedure produces an $N_\mathrm{o} \times N_\mathrm{o}$ unitary, $u^\dagger = (\prod_{\alpha=1}^{(B-1)(N_o - \frac{B}{2})} u_\alpha)^\dagger$, consisting of a ladder of 2×2 single-particle unitaries labeled by ordered index α, which approximately diagonalizes the Green's function. Alternatively, read in reverse, the inverse transformation u approximately converts a product state of (un)occupied sites into the correlated ground-state of h. These single-particle (size $n \times n$) operations can be converted into a circuit acting on the many-particle Hilbert space (of size 2^n) by replacing each 2×2 unitary, u_α, by an equivalent two-qubit gate: $U_\alpha = \exp\left[\sum_{ij} c_i^\dagger (\log u)_{ij} c_j\right] = \exp\left[\sum_{ij} \sigma_i^+ (\log u)_{ij} \sigma_j^-\right]$, where in the second line we have used that the rotation always occurs between neighboring sites and therefore doesn't involve a Jordan Wigner string.

Crucially, the resulting ladder-circuit $U = \prod_\alpha U_\alpha$ can be interpreted as a qMPS with bond dimension $\chi = 2^B$ by chopping it into diagonal causal slices (see Fig. 1), and interpreting the qubit lines entering the bottom of the slice as physical qubits and those entering the side as bond-qubits. We will refer to the resulting MPS as a Gaussian MPS (GMPS) to distinguish it from generic non-Gaussian (q)MPS of the same bond dimension.

Whereas an arbitrary Gaussian state can be prepared by a ladder circuit acting on N_o qubits with $O(N_\mathrm{o}^2)$ two-qubit gates (see for example [17, 18]), the compressed GMPS *ground-state* requires $O(N_\mathrm{o} B)$ two-qubit gates acting on $O(B)$ qubits (if implemented holographically). The efficiency of this compression therefore depends on the block size B required to accurately approximate the state in question. Empirical numerical evidence and entanglement-based arguments indicate that GMPS for ground-states of local Hamiltonians in 1d systems of length L and for target error threshold $\epsilon = 1 - \frac{1}{L}\sum_{i,j} |G_{ij}^{(\mathrm{GMPS})} - G_{ij}|$ requires block size (equivalently number of qubits) $B \sim \log \epsilon^{-1}$ for a gapped state or $B \sim \log L \log \epsilon^{-1}$ for a gapless metallic state. In Appendix D we extend these results to d-dimensional systems, and find that generically B scales with the bipartite entanglement entropy $S(L)$:

$$B \sim S(L) \sim \begin{cases} L^{d-1} \log \epsilon^{-1} & \text{gapped} \\ L^{d-1} \log L \log \epsilon^{-1} & \text{Fermi-surface} \end{cases}, \quad (3)$$

where d is the number of spatial dimensions[1]. This result holds even for topologically non-trivial Chern band insulators that have an obstruction to forming a fully localized Wannier-basis. Combined with "holographic" simulation methods using mid-circuit measurement and reuse, this method dramatically reduces the number of qubits required ($L^{d-1}B$ vs. L^d) to implement the GMPS on a quantum computer.

Trapped-ion GMPS implementation – To demonstrate the feasibility of this approach for near-term hardware, we prepare an entangled metallic ground-state of a spinless non-interacting two-leg ladder (2ll) described by Eq. 2 without spin, and with $L_x = 8, L_y = 2, U = 0$ and $N = 8$ electrons (half-filling). This system has the same number of degrees of freedom of a spinful $L_x = 8$ FH chain that we will be ultimately interested in, but avoids the trivial decoupling of spin-species that arises in mean-field ground-states of the FH chain. The qMPS representation of the compressed GMPS is implemented on Quantinuum's System Model H1 trapped-ion quantum computer utilizing 6 trapped-ion qubits corresponding to block size $B = 2 \times 3$, sufficient to reduce the theoretical compression error below 1%. Using only a simple error mitigation scheme based on post-selecting data with the correct total electron number (see Appendix A for details), we achieve close quantitative agreement (within statistical error bars) between the experimental correlation functions and their theoretical values (see Fig. 1).

[1] We note that these asymptotic expressions are asymptotic in L and assume non-zero density of particles. For finite-size molecules there may be individual orbitals that add extra overhead.

Correlated electron models – Since non-interacting fermion systems permit efficient classical simulation, the GMPS technique is not directly useful by itself. However, holographic qMPS approximations to mean-field states can be helpful starting points for approximating correlated ground states either by i) adiabatic evolution to a correlated system in the same phase as the mean-field state (using efficient holographic time-evolution methods [7]), or ii) reducing the complexity of variational state preparation by providing a good initial guess. Here, we focus on approach ii) and show that relatively simple variational-circuit extensions of the GMPS circuit, which we refer to as GMPS+U methods, provide good approximations to interacting fermion ground-states of a spinful Fermi-Hubbard (FH) chain (Eq. 2 with $L_y = 1$). Since this model can be exactly solved by Bethe-Ansatz methods, this provides a convenient analytic benchmark for the qMPS methods.

Focusing on $U/t = 4$, and half-filling (one electron per site), we first construct a GMPS circuit corresponding to the antiferromagnetic Hartree-Fock (AFM-HF) ground-state with AFM order-parameter: $\mathcal{N} = (-1)^j \langle S^z_j \rangle \neq 0$. We then augment the GMPS-circuitry with a single extra variational circuit layer, which builds in spin-correlations representing quantum fluctuations that wash out the AFM order on long distances. We will refer to the general method of variationally-augmenting GMPS circuits as GMPS+U, and the specific ansatz in Fig. 4a as $(\mathrm{GMPS}+\mathrm{U})_{\mathrm{H}}$. Details of the variational circuit architectures can be found in Appendix C and Fig. 4. Physically, the $(\mathrm{GMPS}+\mathrm{U})_{\mathrm{H}}$ ansatz can be understood as follows: read in reverse, the GMPS circuit (blue gates) approximately maps the Wannier-orbital spins of the AFM-HF bands onto a product state of alternating up and down spins on single qubits. In this disentangled basis basis, these spins approximately form a Heisenberg spin-chain. The extra variational circuit layer (gray box in Fig. 4a) is then closely modeled after the single-parameter variational circuit used in [7] to prepare the highly-entangled Heisenberg chain ground-state. Fig. 2 and Fig. 3 show the energies and correlation functions from experiment and numerical simulations for this GMPS+U ansatz implemented for Fermi-Hubbard model with $L = 6$ spinful fermion sites. Note that the variational form only has one parameter per site, but because it captures the correct physical structure of the ground-state, we recover quite reasonable energies and correlation functions, including the distinct decay of spin- and charge-correlators that is the imprint of spin-charge separation in correlated $1d$ electron systems.

Note that, while the $(\mathrm{GMPS}+\mathrm{U})_{\mathrm{H}}$ ansatz is designed based on the physics of large-U and half-filling, there are many other simple GMPS+U variational ansatzes that can be considered. For example, an ansatz that we will refer to as $(\mathrm{GMPS}+\mathrm{U})_{\mathrm{ZZ}}$, which performs reasonably well for a wide range of interaction strengths and particle-densities (see Appendix G) simply augments each Gaussian fermion gate of the GMPS circuit with an interacting $e^{i\theta_i Z\otimes Z}$ gate with variable θ_i independently for each gate. Numerical simulations (Fig. 2a) show $(\mathrm{GMPS}+\mathrm{U})_{\mathrm{ZZ}}$ obtains significant improvement over the mean-field energy at both large- and small U and at both half- and partial-(1/3) filling (see Appendix. G).

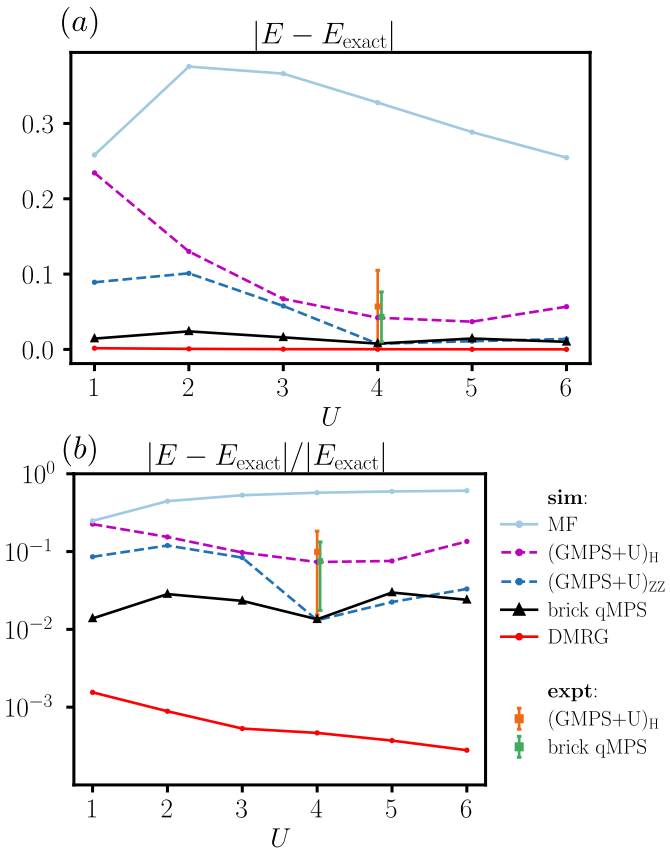

FIG. 2. **Comparison of variational approaches** – to the Fermi-Hubbard chain. Relative error in energy for various variational approaches compared to exact ground-state of the half-filled Fermi-Hubbard chain. Variational approaches include two types of GMPS+U circuits: $(\mathrm{GMPS}+\mathrm{U})_{\mathrm{H}}$ and $(\mathrm{GMPS}+\mathrm{U})_{\mathrm{ZZ}}$ that augment the GMPS with $B = 6$ for the Hartree-Fock ground-state with additional variational circuitry, and a problem-agnostic qMPS ansatz with two bond qubits and four layers of brick circuit (brick qMPS) (see Appendix B for details of circuit ansatzes). For comparison to classical methods, we include, the mean-field (MF) solution, and DMRG results with bond-dimension 2^5 that provide a lower-bound on the achievable energy with $n_b = 5$ bond-qubits used in the $(\mathrm{GMPS}+\mathrm{U})_{\mathrm{H}}$ approach. The number of variational parameters per site are respectively: 1 [$(\mathrm{GMPS}+\mathrm{U})_{\mathrm{H}}$], 6 [$(\mathrm{GMPS}+\mathrm{U})_{\mathrm{ZZ}}$], 80 (brick qMPS), and 1024 (DMRG with $\chi = 2^5$).

Discussion – In this work, we introduced and experimentally demonstrated holographic approaches to prepare ground-states of correlated electron systems. In particular, the efficient preparation of gapped and gapless mean-field ground states as qMPS (obtained by our qMPS adaptation of the GMPS compression scheme of Fishman and White) in conjunction with holographic

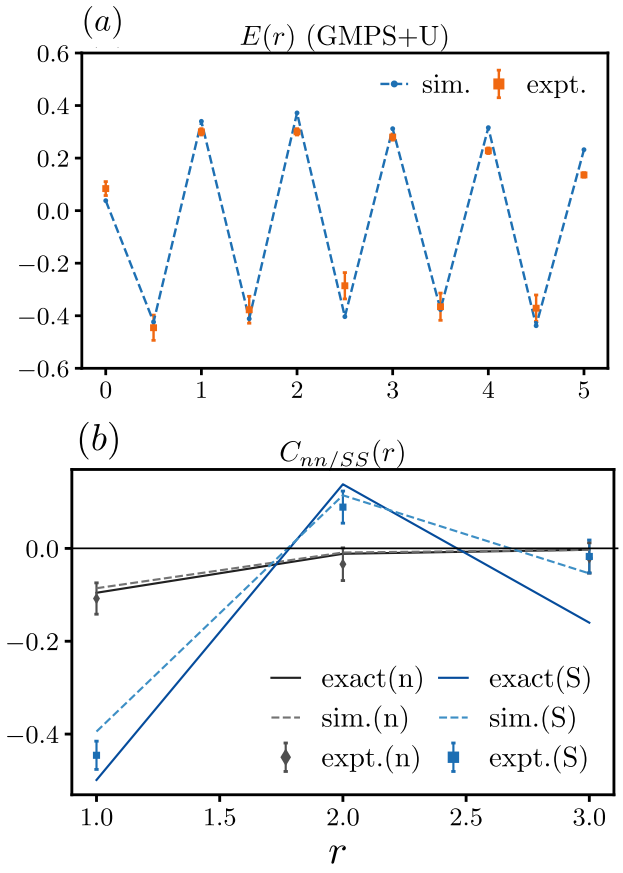

FIG. 3. **GMPS+U Hardware Implementation** – for the Fermi-Hubbard chain at half-filling with U=4. (a) shows energy density versus position in the $(\text{GMPS} + \text{U})_{\text{H}}$ ansatz (which is not explicitly translation invariant), with hopping energies shown at half-integer (bond-centered) positions. (b) Connected spin- (S) and charge-density- (n) correlators show spin-charge separation with rapid decay of charge and slower (antiferromagnetically modulated) decay of spin correlations.

time-evolution algorithms [7], formally establish that qMPS with efficient circuit resources (i.e. scaling polynomially with system size) can accurately capture any state that is continuously connected to a mean-field fermion state (possibly via a continuous phase transition). This includes most phases of matter relevant to practical material simulations, such as metals, correlated trivial- and topological- insulators, magnets, superconductors, density-wave states, et cetera.

Compared to standard adiabatic state preparation protocols, the combination of the holographic approach, qMPS encoding, and Gaussian compression brings important advantages. These manifest already in the mean-field state preparation. For example, for gapped Hamiltonians, the holographic qMPS encoding offers a polynomial reduction in qubit resources (from $q \sim L^d$ to $q \sim L^{d-1}$), and for $2d$ topological systems with nontrivial Chern number further allows a polynomial reduction in gate count (from $g \sim L^4$ to $g \sim L$). Similarly, compared to the Givens rotation approach used in recent hardware demonstrations of Hartree-Fock ground-state preparation [18] which required $q \sim L$ qubits and $g \sim L^2$ gates, qMPS constructed via GMPS compression require only $q \sim \log L \log \epsilon^{-1}$ and $g \sim L \log L \log \epsilon^{-1}$, achieving a polynomial reduction in both resources [2]. Previously, the most efficient Gaussian state preparation protocol was the fermionic Fast Fourier transform (FFFT), which similarly uses $g \sim L \log L$ [19] gates; however, unlike the GMPS technique, it is restricted to translation invariant (plane-wave like) states and requires long-range gates that spoil the holographic savings in qubit number (and may be expensive to implement in many architectures). The source of the efficiency of Gaussian compression is the exploitation of the near-area-law entanglement behavior of physical gapped and gapless ground-states. Retaining this structure in the qMPS then allows for compact preparation of near-area-law interacting ground-states. We demonstrated this here by preparing ground-states of interacting 1D fermion Hamiltonians, including those with extended power-law ground-state correlations in G_{ij}, using GMPS+U circuits adapted from the mean-field circuits.

Natural targets for follow on work include tackling higher-dimensional systems via $2d$ or $3d$ qMPS or qTNS techniques, exploring alternative fermion-to-qubit encodings that are well-suited to qTNS methods, and exploring qTNS-based embedding techniques [20] to simulate realistic material models with complex (e.g. long-range) interactions.

Acknowledgements – We thank Itamar Kimchi, Roger Mong, and Michael Zaletel for insightful conversations. We acknowledge support from NSF award DMR-2038032 (YZ, AP), NSF-Converence Accelerator Track C award DMR- (DN, GKC), from the Alfred P. Sloan Foundation through a Sloan Research Fellowship (AP). RH was supported by the US Department of Energy, Office of Science, via Award No. DE-SC0019374. Additional support from GKC was provide by the Simons Collaboration on the Many-electron Problem and the Simons Investigatorship. This research was undertaken thanks, in part, to funding from the Max Planck-UBC-UTokyo Center for Quantum Materials and the Canada First Research Excellence Fund, Quantum Materials and Future Technologies Program. Numerical calculations were performed using supercomputing resources at the Texas Advanced Computing Center (TACC).

[2] We note that the gate count gains are asymptotic, for the task of simulating a spinful $L_x = 8$ FH chain, both methods require nearly the same number of entangling gates (130 Mølmer-Sørensen gates for GMPS versus 128 $\sqrt{\text{iSWAP}}$ gates for given rotations).

[1] Frank Arute, Kunal Arya, Ryan Babbush, Dave Bacon, Joseph Bardin, Rami Barends, Rupak Biswas, Sergio Boixo, Fernando Brandao, David Buell, Brian Burkett, Yu Chen, Zijun Chen, Ben Chiaro, Roberto Collins, William Courtney, Andrew Dunsworth, Edward Farhi, Brooks Foxen, and John Martinis, "Quantum supremacy using a programmable superconducting processor," Nature **574**, 505–510 (2019).

[2] Han-Sen Zhong, Hui Wang, Yu-Hao Deng, Ming-Cheng Chen, Li-Chao Peng, Yi-Han Luo, Jian Qin, Dian Wu, Xing Ding, Yi Hu, *et al.*, "Quantum computational advantage using photons," Science **370**, 1460–1463 (2020).

[3] Scott Aaronson and Alex Arkhipov, "The computational complexity of linear optics," in *Proceedings of the forty-third annual ACM symposium on Theory of computing* (2011) pp. 333–342.

[4] Bela Bauer, Sergey Bravyi, Mario Motta, and Garnet Kin-Lic Chan, "Quantum algorithms for quantum chemistry and quantum materials science," Chemical Reviews **120**, 12685–12717 (2020).

[5] Ulrich Schollwöck, "The density-matrix renormalization group in the age of matrix product states," Annals of physics **326**, 96–192 (2011).

[6] F Barratt, James Dborin, Matthias Bal, Vid Stojevic, Frank Pollmann, and AG Green, "Parallel quantum simulation of large systems on small nisq computers," npj Quantum Information **7**, 1–7 (2021).

[7] Michael Foss-Feig, David Hayes, Joan M Dreiling, Caroline Figgatt, John P Gaebler, Steven A Moses, Juan M Pino, and Andrew C Potter, "Holographic quantum algorithms for simulating correlated spin systems," Physical Review Research **3**, 033002 (2021).

[8] Sheng-Hsuan Lin, Rohit Dilip, Andrew G Green, Adam Smith, and Frank Pollmann, "Real-and imaginary-time evolution with compressed quantum circuits," PRX Quantum **2**, 010342 (2021).

[9] Michael Foss-Feig, Stephen Ragole, Andrew Potter, Joan Dreiling, Caroline Figgatt, John Gaebler, Alex Hall, Steven Moses, Juan Pino, Ben Spaun, *et al.*, "Entanglement from tensor networks on a trapped-ion qccd quantum computer," arXiv preprint arXiv:2104.11235 (2021).

[10] Eli Chertkov, Justin Bohnet, David Francois, John Gaebler, Dan Gresh, Aaron Hankin, Kenny Lee, Ra'anan Tobey, David Hayes, Brian Neyenhuis, *et al.*, "Holographic dynamics simulations with a trapped ion quantum computer," arXiv preprint arXiv:2105.09324 (2021).

[11] Lucas Slattery and Bryan K Clark, "Quantum circuits for two-dimensional isometric tensor networks," arXiv preprint arXiv:2108.02792 (2021).

[12] Ian MacCormack, Alexey Galda, and Adam L Lyon, "Simulating large peps tensor networks on small quantum devices," arXiv preprint arXiv:2110.00507 (2021).

[13] Isaac H Kim, "Holographic quantum simulation," arXiv preprint arXiv:1702.02093 (2017).

[14] Matthew T Fishman and Steven R White, "Compression of correlation matrices and an efficient method for forming matrix product states of fermionic gaussian states," Physical Review B **92**, 075132 (2015).

[15] David Perez-Garcia, Frank Verstraete, Michael M Wolf, and J Ignacio Cirac, "Matrix product state representations," arXiv preprint quant-ph/0608197 (2006).

[16] Laszlo Gyongyosi and Sandor Imre, "Properties of the quantum channel," arXiv preprint arXiv:1208.1270 (2012).

[17] Ian D Kivlichan, Jarrod McClean, Nathan Wiebe, Craig Gidney, Alán Aspuru-Guzik, Garnet Kin-Lic Chan, and Ryan Babbush, "Quantum simulation of electronic structure with linear depth and connectivity," Physical review letters **120**, 110501 (2018).

[18] Frank Arute, Kunal Arya, Ryan Babbush, Dave Bacon, Joseph C Bardin, Rami Barends, Sergio Boixo, Michael Broughton, Bob B Buckley, David A Buell, *et al.*, "Hartree-fock on a superconducting qubit quantum computer," Science **369**, 1084–1089 (2020).

[19] Andrew J Ferris, "Fourier transform for fermionic systems and the spectral tensor network," Physical review letters **113**, 010401 (2014).

[20] Reza Haghshenas, Johnnie Gray, Andrew C. Potter, and Garnet Kin-Lic Chan, "The variational power of quantum circuit tensor networks," (2021), arXiv:2107.01307 [quant-ph].

[21] Juan M Pino, Jennifer M Dreiling, Caroline Figgatt, John P Gaebler, Steven A Moses, MS Allman, CH Baldwin, M Foss-Feig, D Hayes, K Mayer, *et al.*, "Demonstration of the trapped-ion quantum ccd computer architecture," Nature **592**, 209–213 (2021).

[22] Johnnie Gray, "quimb: a python library for quantum information and many-body calculations," Journal of Open Source Software **3**, 819 (2018).

[23] Titus Neupert, Luiz Santos, Claudio Chamon, and Christopher Mudry, "Fractional quantum hall states at zero magnetic field," Physical review letters **106**, 236804 (2011).

[24] Michael M Wolf, Frank Verstraete, Matthew B Hastings, and J Ignacio Cirac, "Area laws in quantum systems: mutual information and correlations," Physical review letters **100**, 070502 (2008).

[25] Jirí Guth Jarkovskỳ, András Molnár, Norbert Schuch, and J Ignacio Cirac, "Efficient description of many-body systems with matrix product density operators," PRX Quantum **1**, 010304 (2020).

[26] Rajibul Islam, Ruichao Ma, Philipp M Preiss, M Eric Tai, Alexander Lukin, Matthew Rispoli, and Markus Greiner, "Measuring entanglement entropy in a quantum many-body system," Nature **528**, 77–83 (2015).

[27] Tiff Brydges, Andreas Elben, Petar Jurcevic, Benoît Vermersch, Christine Maier, Ben P Lanyon, Peter Zoller, Rainer Blatt, and Christian F Roos, "Probing rényi entanglement entropy via randomized measurements," Science **364**, 260–263 (2019).

[28] John Martyn and Brian Swingle, "Product spectrum ansatz and the simplicity of thermal states," Physical Review A **100**, 032107 (2019).

[29] Philippe Corboz and Guifré Vidal, "Fermionic multiscale entanglement renormalization ansatz," Physical Review B **80**, 165129 (2009).

Supplemental Information

A. Quantinuum QCCD Architecture

Hardware implementations are performed on Quantinuum's System Model H1 trapped-ion quantum processor [21], which uses a quantum charge-coupled device (QCCD) arthiceture, based on a Honeywell-fabricated planar chip trap operating with three parallel gate zones and 10 qubit ions. One-qubit ($1q$) gates implement $\pi/2$ rotations about an arbitrary axis in the σ^{xy}-plane. The native entangling two-qubit gate is a Mølmer-Sørensen gate wrapped with single-qubit dressing pulses to achieve a phase-insensitive operation $u_{MS} = \exp[-i\frac{\pi}{4}\sigma^z \bigotimes \sigma^z]$ [21]. The one-qubit gates and two-qubit gates have typical average infidelities (determined by randomized benchmarking techniques) of: $\epsilon_{1q} \approx 10^{-4}$ and $\epsilon_{2q} \approx 2-5\times10^{-3}$.

Due to the large sampling overhead and relatively low clock speed of the QCCD device, we chose to only perform part of the holographic variational quantum eigensolver (holoVQE) algorithms on the quantum device. Namely, in all cases, we performed the variational optimization of circuit parameters through classical simulations, and implemented only the optimized circuit in hardware. While this procedure does not address the effect of hardware noise on the variational optimization (nor allow for possible variational cancellation of coherent errors), it nevertheless allows one to test how realistic hardware errors affect the achievable variational errors with different circuit types.

B. GMPS Circuit implementations

In the GMPS compression algorithm, a basis transformation specified from the eigenvector of the Green's function block transfers the least entangled states to the first site of the block. The corresponding basis transformation is decomposed into a series of nearest neighbor two-site gates which rotate the Green's function block into the occupation basis. The circuit and gate parameters are obtained from the eigenvectors.

Rotating the first site to the eigenvector $(v_1, v_2, ..., v_{B-1}, v_B)$ requires $(B-1)$ two-site gates in total. The first gate acts on site $(B-1, B)$ and is labeled as V_{B-1}. V_{B-1} satisfies $v^T V_{B-1} = (v_1, ...v'_{B-1}, 0)$. In general the gate V_i satisfies $(v_1, ...v'_{i+1}, 0, ...0)^T V_i = (v_1, ..., v'_i, 0, ...0)$ and it takes the form:

$$V_i = V(\theta_i) = \begin{pmatrix} \cos\theta_i & -\sin\theta_i \exp(i\phi_i) \\ \sin\theta_i \exp(-i\phi_i) & \cos\theta_i \end{pmatrix} \tag{B1}$$

When the Green's function is real, $\phi = 0$ and $\theta_{B-1} = \tan^{-1}(v_B/v_{B-1})$, thus the gate V_i takes the same form as in Ref. [14] When the Green's function is complex in certain cases (like in Chern insulators), the eigenvectors are also complex thus the extra phase factor ϕ becomes necessary. The entries of the Green's function are updated once the gate acts on it. The next gate acts on $(B-2, B-1)$ and so on. This procedure gives us V_{B-1}, V_{B-2},...,V_1. The total unitary transformation is $V_{\mathcal{B}_1} = V_{B-1}V_{B-2}...V_1$. Acting this on the Green's function G yields the transformed Green's function $V^\dagger_{\mathcal{B}_1} G V_{\mathcal{B}_1}$ with $n_1 \approx 0$ or 1. The procedure is repeated for sites 2,... $B+1$ to obtain $V_{\mathcal{B}_2}$. For the last few sites, the block size becomes the number of the remaining sites. In the end we obtain the total unitary transformation $V = V_{\mathcal{B}_1} V_{\mathcal{B}_2} ... V_{\mathcal{B}_{N-1}}$.

C. Variational Circuit Architectures

This subsection details the architecture for the variational circuits shown in Fig. 4. This includes two types of GMPS+U circuits that augment the GMPS Hartree-Fock circuit with additional variational circuits:
i) the $(\text{GMPS}+\text{U})_\text{H}$ ansatz (where 'H' stands for 'Heisenberg') depicted in Fig. 4a) geared towards large-U and half-filling, and
ii) the $(\text{GMPS}+\text{U})_{\text{ZZ}}$ ansatz (Fig. 4b) which is agnostic to filling and U (although it tends to perform best at large or small U), and
iii) a problem-agnostic brick circuit (Fig. 4c), which can achieve great accuracy, but at the cost of introducing a comparatively large number of variational parameters.

1. $\text{GMPS}+\text{U}_\text{H}$

The $\text{GMPS}+\text{U}_\text{H}$ ansatz exploits the physical picture that the half-filled Fermi-Hubbard model behaves like a Heisenberg spin-chain at large-U, by introducing a variational "pre-entangling" circuit before the GMPS circuitry (Fig. 4a) using a single extra bond-qubit and layer of variational gates to build in quantum fluctuations of the AFM spin-texture in the Hartree-Fock ground-state. The aim is to emulate a qMPS state of the electron spins without altering the charge state. In our approach, we encode each spinful fermion site into two qubits whose computational basis encodes the particle occupation number of the up and down spin orbitals: $|n_\uparrow, n_\downarrow\rangle$. The input state to the GMPS circuit is simply a product state of Fermi-Hubbard sites with a single particle on each site, and with spin alternating between up and down. To entangle the spin- degrees of freedom on different sites without

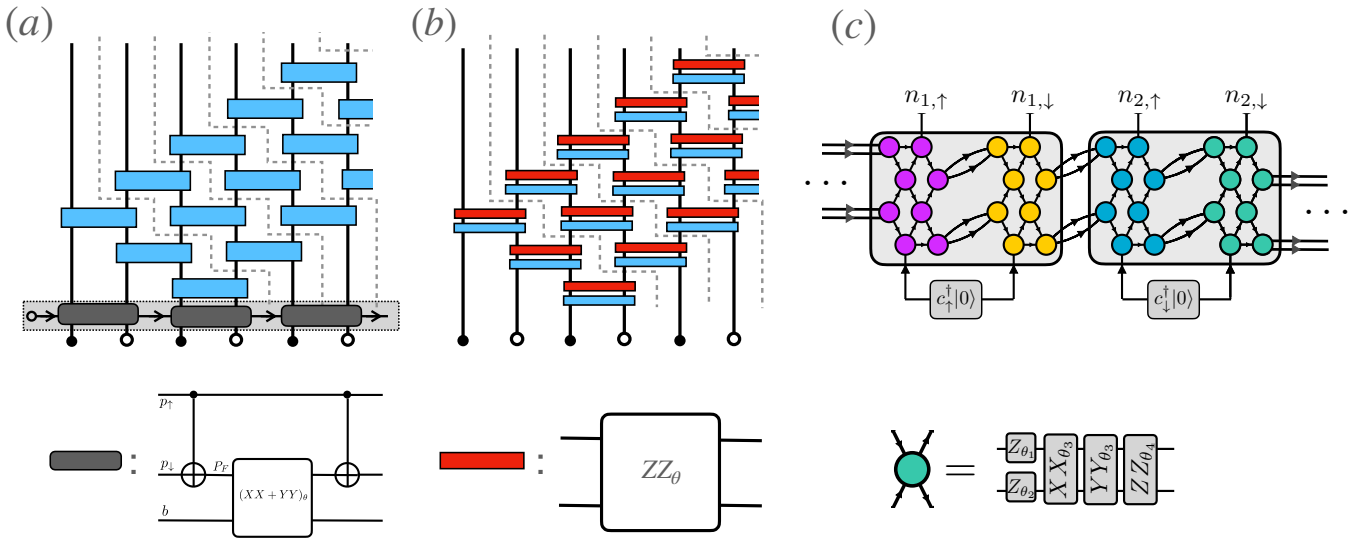

FIG. 4. **Variational circuit architectures**: Correlations can be added either by (a) GMPS + U_H: introducing an extra qMPS layer with an extra bond-qubit (gray dashed box) or by (b) GMPS + U_{zz}: generalizing the GMPS gates (blue boxes) to include non-Gaussian operations. Here we draw the GMPS+U circuits only for block-size $B = 3$ (the implemented circuits have twice this block size, $B = 6$ to include spin). An alternative way is to implement (c) holoVQE on a qMPS ansatz.

affecting their charge, we employ a basis transformation using a CNOT gate, which corresponds to the following map:

$$\begin{aligned} |n_\uparrow, n_\downarrow\rangle &\longrightarrow |\text{flavor}, 2P_F - 1\rangle : \\ |0,0\rangle &\longrightarrow |0,0\rangle \\ |0,1\rangle &\longrightarrow |0,1\rangle \\ |1,0\rangle &\longrightarrow |1,1\rangle \\ |1,1\rangle &\longrightarrow |1,0\rangle. \end{aligned} \tag{C1}$$

In the transformed basis the second qubit encodes the even/odd fermion parity $P_F = (-1)^{n_\uparrow + n_\downarrow}$. The flavor qubit's interpretation depends on the value of P_F. When P_F is odd, there is a single electron per site and the first qubit's Pauli operators correspond to the electron spin operator, e.g. $Z_1 = c_s^\dagger \sigma^z_{ss'} c_{s'}$ (and similarly for Y, Z). While our initial states will always have odd fermion parity, for completeness, we mention that for even fermion parity the "flavor" qubit encodes the occupation number of a spin-singlet Cooper pair created by $c_\uparrow^\dagger c_\downarrow^\dagger$.

In the flavor/parity basis, the electron-spin on each site now maps to the state of a single qubit, and we can apply a variational $XX + YY$ gate

$$u_{\text{XX+YY}}(\theta) = \exp\left[-i\frac{\theta}{2}(X \otimes X + Y \otimes Y)\right] \tag{C2}$$

between this flavor qubit and an extra bond qubit, emulating the variational circuitry for a qMPS approximation to the Heisenberg spin-chain ground-state explored in [7]. We then transform back to the original particle occupancy basis to implement the GMPS circuit for the Hartree-Fock ground-state. The $(\text{GMPS} + \text{U})_\text{H}$ circuit introduces only a single extra variational parameter per site.

2. GMPS + U_{ZZ}

In the $(\text{GMPS} + \text{U})_{\text{ZZ}}$ ansatz, we simply add an additional variable-rotation $u_{zz}(\theta_i) = e^{-\frac{i}{2}\theta_i Z \otimes Z}$ gate to each of the free-fermion GMPS gates, with independent variational parameters θ_i for each gate. These gates are non-Gaussian for generic values of θ, and produces a correlated non-Gaussian fermion qMPS. The number of variational parameters in this ansatz is equal to the number, $(\sim N_o B)$, of two-qubit gates in the GMPS circuit.

3. Brick circuit qMPS

Besides the GMPS+U approaches, we also employ a problem-agnostic variational circuit approach, which we will label by the term brick qMPS. Specifically, we fix a brickwork circuit architecture with general particle-number conserving two-qubit gates (see Fig. 4) to generate the tensors of a qMPS with $\chi = 2^4$ and classically minimize $\langle H_{\text{FH}} \rangle$ with respect to the variational parameters using quimb [22]. The number of bond-qubits and gates in this ansatz can be arbitrarily scaled to achieve larger expressiveness. However, this introduces a large number of variational parameters (5 parameters per two-qubit gate), which may be difficult to train on larger problem instances (e.g. $2d$ models).

Our brickwork circuit ansatz employs general particle number-conserving two-qubit gates to enable noise mit-

igation based on post-selecting the data on having the correct total particle number, with unitary:

$$\begin{pmatrix} e^{i(\gamma+\phi)} & 0 & 0 & 0 \\ 0 & e^{i(-\gamma+\phi+\zeta)}\sin\theta & e^{-i(\chi+\gamma+\phi)}\cos\theta & 0 \\ 0 & e^{i(\chi-\gamma+\phi)}\cos\theta & e^{-i(\gamma+\phi+\zeta)}\sin\theta & 0 \\ 0 & 0 & 0 & e^{i(\gamma-\phi)} \end{pmatrix} \tag{C3}$$

where $(\gamma, \phi, \zeta, \chi, \theta)$ are variational parameters (independently chosen for each two-qubit gate in Fig. 4c).

4. Noise mitigation

As a simple noise mitigation method, we post-select our data on having the correct total particle number. Since a noiseless implementation of the circuits used conserves total particle number, any deviation from the ideal number can only be caused by gate errors (though not vice versa). This symmetry-based postselection gives a modest but noticeable improvement in measuring the Green's functions and density correlations. An example is shown in Fig. 5, comparing the measurement results with and without the noise mitigation.

When all the measurements are in the Pauli-Z bases, it is convenient to keep track of the particle number just using the measurement results. The most straightforward way of measuring Green's functions $\langle c^\dagger_{r_1} c_{r_2}\rangle$, would be to implement separate measurements of its real and imaginary parts as Pauli strings: "...XZ...Z...ZX..." and "...YZ...Z...ZY...". However, as these strings do not individually commute with total particle number, the method would be incompatible with our error mitigation scheme. Instead, we add additional gates to map $X_iX_j+Y_iY_j$ and Z_i+Z_j eigenstates to the computational basis so that the real part of G and the total number can be simultaneously measured. This mapping is achieved by the unitary (written in the Z_i, Z_j eigenbasis):

$$U_M = \begin{pmatrix} 1 & 0 & 0 & 0 \\ 0 & \frac{1}{\sqrt{2}} & \frac{1}{\sqrt{2}} & 0 \\ 0 & \frac{1}{\sqrt{2}} & -\frac{1}{\sqrt{2}} & 0 \\ 0 & 0 & 0 & 1 \end{pmatrix}. \tag{C4}$$

Since the state is built sequentially from left to right, performing this rotation requires postponing the mid-circuit measurement and reset of the qubit at r_1 until site r_2 is reached, which requires a single extra hardware qubit compared to the basic qMPS circuit without error mitigation.

D. Resource scaling of GMPS compression in $2d$

The GMPS method was originally developed for $1d$ systems. Here we consider its extension to higher-dimensions, focusing on $2d$, by adopting an approach similar to that of $2d$-DMRG where a quasi-$2d$ system

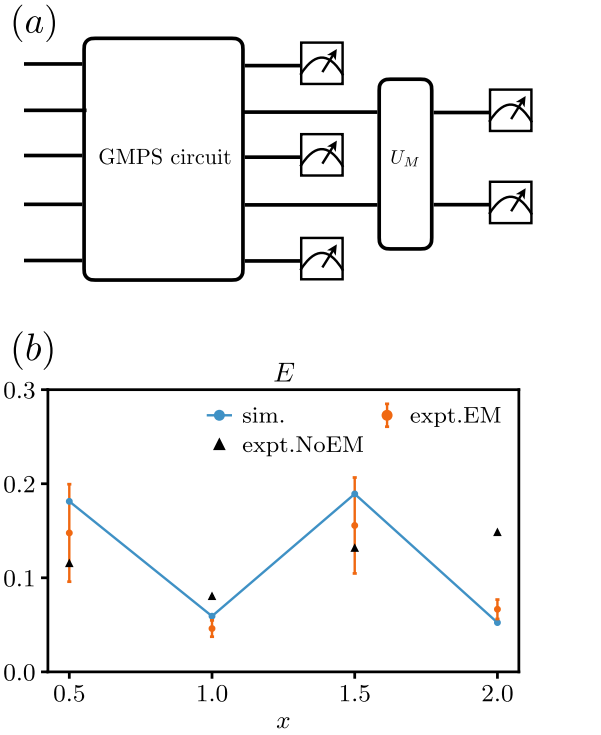

FIG. 5. **Noise mitigation** – (a) To mitigate noise, we postselect on results with the correct total particle number. To simultaneously measure total particle number and Green's function elements $\langle c^\dagger_i c_j\rangle$, we add a basis transformation gate U_M for the corresponding qubits of the Green's functions before measuring them and each qubit is measured in the Pauli Z basis. In the holographic implementation, the first qubit being measured cannot be reset and reused until both sites are i, j are measured. (b) A comparison between measurement results for qMPS VQE method of U=6, half-filled Fermi-Hubbard model with (EM) and without (NoEM) the error mitigation.

of length L_x and width L_y is considered as a stack of L_x "slices". Through numerical simulations, we empirically investigate the resource scaling required to implement GMPS representations of three important classes of states (see Fig. 6:

1. a topologically-trivial 1d band-insulator (L_y=1) is constructed from the Su-Schreifer-Heeger (SSH) model with Hamiltonian $H_{\rm SSH} = \sum_{i=1}^{\frac{N-1}{2}}(-t(1+\frac{\delta}{2})a^\dagger_{2i-1}a_{2i} - t(1-\frac{\delta}{2})a^\dagger_{2i}a_{2i+1} + h.c.)$ with $\delta = 1$,

2. a topologically-nontrivial Chern-insulator is constructed from the ground-state of a square-lattice π-flux tight-binding model of [23], with parameter t_1=1, t_2=1 and the periodic boundary condition in L_y direction (to avoid gapless chiral edge states along the cylinder), and

3. a two-dimensional metal with a Fermi-surface from an isotropic tight-binding is constructed from the gorund-state of a square lattice tight-binding

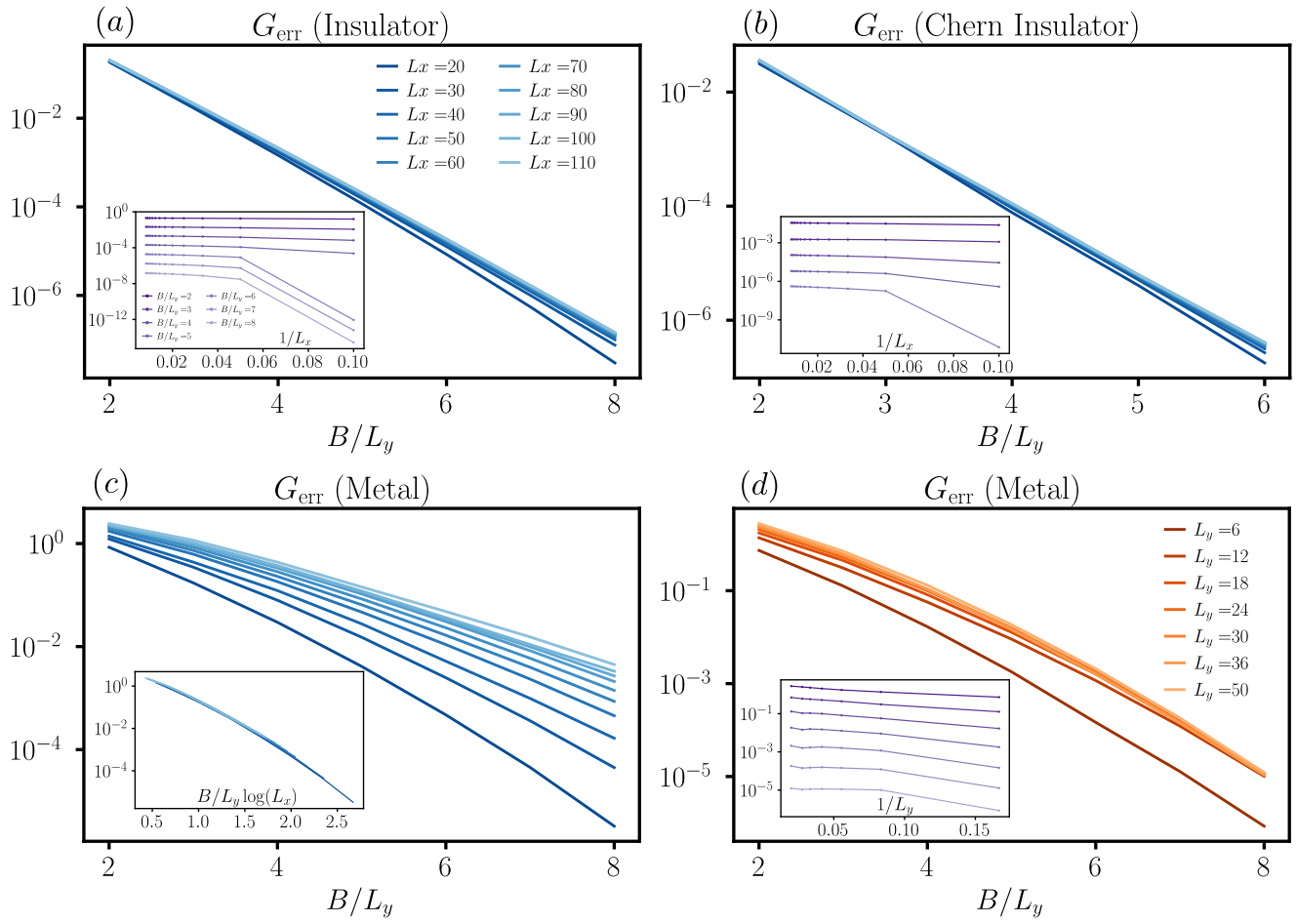

FIG. 6. **GMPS compression resource scaling**: (a)-(d) show the mean error $G_{\rm err}$ of Green's functions versus the GMPS compression block size for various systems and system sizes. $G_{\rm err}$ is defined by $G_{\rm err} = \sum_{i,j} |G^c_{i,j} - G^o_{i,j}|/V$, where G^o and G^c are the original and compressed Green's function and V is the system size. In each plot we stop at the block size when the eigenvalues cannot be improved by increasing block size as it already reaches the limit of machine precision 10^{-15}. (a)-(c) show the error versus the block sizes for different L_x while L_y is fixed (to 1,6,6); (d) shows the compression error versus the block sizes for different L_y with $L_x = 50$. The inset of (a), (b), (d) show the the $G_{\rm err}$ versus $1/L_x$ or $1/L_y$. The inset of (c) shows the $C_{\rm err}$ versus the block size re-scaled by $\log(L_x)$.

Hamiltonian $H = \sum_{\langle i,j\rangle}(-tc_i^\dagger c_j + h.c.)$ where $\langle\rangle$ denotes the neighboring sites, with the periodic boundary condition in L_y direction

We measure the quality of the GMPS approximation via the mean error in the entries of G_{ij} and focus on the regime where the eigenvalues obtained in the GMPS approximation can be improved until machine precision by using larger block sizes. In each case, we provide numerical evidence that the block-size required for GMPS compression scheme follows that expected by the entanglement structure of these states, namely to achieve error ϵ requires $B \sim L_y \log(1/\epsilon)$ for both topological and trivial insulating states, and $B \sim L_y \log L_x \log(1/\epsilon)$ for metals, which is consistent with $B \sim S(L_x, L_y)$ where $S(L_x, L_y)$ is the half-system bipartite entanglement entropy.

The Chern insulator result may initially seem surprising, since non-zero Chern number provides a fundamental obstruction to forming a localized Wannier basis, and at first glance the GMPS algorithm may appear to be constructing such a basis. However, we note two points. First, the quasi-1d GMPS circuit structure only has locality along x, whereas the Chern obstruction only forbids simultaneous localization in both x and y directions. Specifically, the projection of the spatial coordinate into the orbitals of a Chern band $(\hat{X}, \hat{Y})$ fail to commute $[X, Y] \sim C$ where C is the Chern number. Second, we have seen the GMPS circuit with $B \sim \log L_x$ is accurate even for a metals with Fermi-surfaces where the Wannier orbitals have algebraic decay in space. This indicates that the GMPS circuit *cannot* simply be understood as a mapping to a strictly local Wannier basis. Technically, the unitary basis transformation implemented by the GMPS circuit is an upper triangular matrix and can produce long-range tails in the later entries.

One significant consequence of this result is that it implies a polynomial advantage of qMPS techniques for simulating correlated Chern insulators compared to standard quantum simulation protocols (e.g. using adiabatic state preparation). Specifically, the number of gates required to prepare a non-interacting Chern-insulator ground-state via the GMPS method is $G \sim BL_x \sim L_yL_x \sim L^2$, and any correlated Chern insulator that is adiabatically connected to the non-interacting limit could be reached with constant overhead via holographic time-evolution [7]. By contrast adiabatic state preparation of the Chern insulator from an un-entangled product state would require $G \sim L_yL_x/\Delta_{\min}(L_x, L_y)^2 \sim L^4$ where $\Delta_{\min} \sim 1/\min(L_x, L_y)$ is the minimal gap encountered in the adiabatic preparation sequence. The numerical simulations further complete the claim that the compression algorithm can work for any GMPS.

E. GMPS for superconductors and thermal states

While Ref. [14] focused on classical GMPS method for ground-states of real, number conserving free-fermion Hamiltonians, it is straightforward to generalize this framework to general Gaussian fermion pure- and mixed-states. The case of complex Hamiltonian entries is already accounted for by the phases, ϕ in equation Eq. B1 above. Below we briefly sketch the generalizations for superconducting and mixed (e.g. thermal) Gaussian states.

1. Particle Non-Conserving States (Superconductors)

For superconducting mean-field states that do not conserve particle number, a standard convenient trick is to redundantly represent N fermion orbitals using a $2N$-component Nambu operator:

$$\psi_{i,s} = \left(c_1, \ \ldots c_N, \ c_1^\dagger, \ \ldots \ c_N^\dagger\right)^T \tag{E1}$$

where $s = +1$ corresponds to the particle (c_i) block and $s = -1$ to the hole ($c_i^\dagger$) block. Denoting the Pauli matrices in this particle-hole space as $\vec{\tau}_{ss'}$, this description has a particle-hole redundancy $\psi^\dagger = \tau^1\psi$. The classical part of the GMPS algorithm can then be run as normal in this Nambu basis, except that each time one identifies an approximate block eigenvector $\boldsymbol{v}$ with block occupation number n close to 0 or 1, its particle hole conjugate $\tau^1\vec{v}$ will also be a block eigenvector with the block occupation number $1-n$, which is equally well localized to the block. These vectors should be simultaneously decoupled from the rest of the system by implementing rotations V_B and $\tau^1V_B\tau^1$ on G. In the many-body language the many-body operator corresponding to single-particle rotation V_{ij} is $e^{\psi^\dagger_{is}(\log V)_{is,js'}\psi_{js}}$, which will automatically perform both V_B and $\tau^1V_B\tau^1$ rotations due to the particle-hole redundancy.

2. Thermal states via purifications

It is also possible to prepare a purified version of Gaussian mixed states via GMPS methods at the cost of doubling the number of qubits required compared to a pure Gaussian state. Without loss of generality, we consider this method for thermal states of the form: $\rho = \frac{1}{Z}e^{-c_i^\dagger h_{ij}c_j}$ (where we have chosen normalization of h such that temperature is 1, and Z normalizes $\mathrm{tr}\rho = 1$), since any Gaussian mixed state can be represented in this way. We expect the compression to be effective when h is a local Hamiltonian, since these thermal states will have an area-law scaling of mutual information [24] and efficient matrix-product density operator form [25].

The basic idea is to prepare a thermofield-double (TFD) type state on a doubled system with the fermion creation operators of the system and double respectively labeled as c_i, a_i (here 'a' stands for ancilla). To start, consider just a single mode thermal state $\rho_T = \frac{1}{Z}e^{-\varepsilon c^\dagger c}$. This can be prepared as a TFD state: $|\Psi_{\mathrm{TFD}}\rangle = \frac{1}{\sqrt{Z}}e^{-\varepsilon c^\dagger a/2}|0\rangle_s \otimes |1\rangle_a$, which has the properties i) $\rho_T = \mathrm{tr}_a|\Psi_{\mathrm{TFD}}\rangle\langle\Psi_{\mathrm{TFD}}|$, and ii) $|\Psi_{\mathrm{TFD}}\rangle$ is a Gaussian fermion state that can be approximately prepared as a GMPS acting on the doubled $\{c, a\}$ system. For multiple modes, this simply generalizes to $|\Psi_{\mathrm{TFD}}\rangle = \frac{1}{\sqrt{Z}}e^{-c_i^\dagger h_{ij}a_j}|0\rangle_s \otimes |1\rangle_a$ where $|0\rangle$ is the all-empty state, and $|1\rangle$ is the all-full state respectively (as can be seen by working in the eigenbasis of h_{ij} which reduces to the single-mode problem above).

This Gaussian TFD (GTFD) preparation could be particularly effective as a starting point for variational thermal state preparation schemes based on minimizing the free energy $F = \langle H\rangle - TS$ where $S = -\mathrm{tr}\rho_s \log \rho_s$. Namely, whereas computation of $\langle H\rangle$ for a variational state is straightforward on a quantum computer, measurements of S for an unknown state incur exponential sampling overhead [26, 27]. However, if one starts with a GTFD state, and adds subsequent variational circuit layers acting on the c system alone, the entropy of the c-system remains that of the initial thermal state, which can be efficiently calculated classically. The resulting state has a fine-tuned entanglement spectrum that is the direct product of many independent two-state systems (one per fermion orbital). Generic thermal states instead exhibit random-matrix type entanglement spectrum with level-repulsion between nearby entanglement energies. However, recent work [28] provides evidence and arguments that the fine-details of the entanglement level spacing statistics are not visible in physical quantities of interest such as correlations of local observables, and that product-state entanglement spectrum ansatzes are effective at reproducing such observables in correlated thermal states.

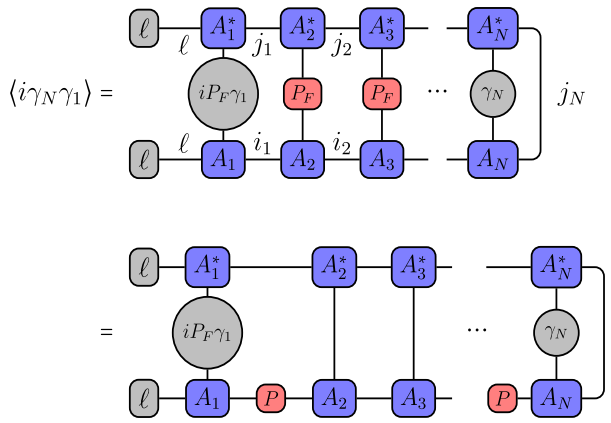

FIG. 7. The schematic representation of applying equation (B1) to fermionic operator $\gamma_{1,N}$

F. Circumventing Jordan-Wigner String Measurements

Measuring fermion correlations between distant sites requires measuring long Jordan-Wigner (JW) strings. Errors in measurement will generically cause such observables to decay exponentially in distance. While this effect is minor for moderate system sizes explored in this paper, it may become a dominant source of error in larger-scale models. Here, we show that in holographic qMPS simulations, it is possible to avoid measurement of long JW strings, by "pulling" the strings back into the virtual bond-space of the MPS (see Appendix A of [29]) where they largely cancel except for additional boundary terms that can be measured by sampling results from a small number of different qMPS contractions.

The measurement of Jordan-Wigner string can be simplified in the following way: first, we pull back the Jordan Wigner strings onto the bond space: Specifically, for tensors that have definite fermion parity, it is always possible to pull back the action of fermion parity operators: $P_{F,i} = (-1)^{n_{F,i}}$ where $n_{F,i}$ is the total number of physical fermions on site i, which appear in the JW string, into operators acting on the input and output bonds of the tensor:

$$(P_F)_s A_s^{ij} = P_{ik}^\dagger A_s^{ij} P_{lj} \tag{F1}$$

where P is the representation of fermion parity on the bond space. Crucially, each bond in the middle of the JW string has a P from the tensor to its left and a $P^\dagger$ from the tensor to its right, which cancel, leaving only P's at the terminal bonds, as shown schematically in Fig. 7.

The transfer matrix with P acting on the lower-leg but not the upper-leg is not a valid quantum channel, but we can decompose it as a linear combination of a small number of quantum channels that can be separately measured, and then linearly combined to compute the desired result. To this end, we introduce the following two basic operations on the bond space. First, denote measurement of bond-fermion parity M_P:

$$\begin{aligned} M_P &= \Pi_{P=1} \otimes \Pi_{P=1} - \Pi_{P=-1} \otimes \Pi_{P=-1} \\ &= \frac{(1+P)}{2} \otimes \frac{(1+P)}{2} - \frac{(1-P)}{2} \otimes \frac{(1-P)}{2} \\ &= \frac{1}{2}\left[P \otimes 1 + 1 \otimes P\right] \end{aligned} \tag{F2}$$

Implementing M_P requires measuring P on the bond register without collapsing the full bond-wave function, which in practice can be done using an ancilla and standard phase-kickback scheme (one of the physical qubits which has already been measured and is currently not active can play this role so that the total qubit resource requirements are unaffected).

Second, we define the operator $\sin(\frac{\pi}{4}\mathrm{ad}_P)$ where $\mathrm{ad}_P \circ = [P, \circ]$:

$$\begin{aligned} \sin\left(\frac{\pi}{4}\mathrm{ad}_P\right) &= \frac{1}{2i}\left(e^{i\frac{\pi}{4}\mathrm{ad}_P} - e^{-i\frac{\pi}{4}\mathrm{ad}_P}\right) \\ &= \frac{1}{2}\left(P \otimes 1 - 1 \otimes P\right), \end{aligned} \tag{F3}$$

and each of the terms: $e^{i\frac{\pi}{4}\mathrm{ad}_P} = e^{\pm i\pi P/4} \otimes e^{\mp i\pi P/4}$ can be implemented simply by applying the unitary operator $e^{\pm i\pi P/4}$ to the bond-qubit register.

From these two ingredients, the desired operation of applying P to the lower bond-legs but not the upper ones can then be written as:

$$P \otimes 1 = M_P + \frac{1}{2i}\left(e^{i\pi P/4} \otimes e^{-i\pi P/4} - e^{-i\pi P/4} \otimes e^{i\pi P/4}\right) \tag{F4}$$

which we have just shown can be expressed as a weighted sum of the results obtained by sampling four different valid quantum channels that can each be implemented holographically.

This method becomes useful in cases where mid-circuit measurement errors are the dominant source of error (as opposed to, say, gate errors building up in the implementation of the qMPS tensors), and becomes helpful when the JW string is sufficiently long that its measurement error exceeds that introduced by the extra circuitry required to perform the M_P and $\sin(\frac{\pi}{4}\mathrm{ad}_P)$ operations.

G. 1/3-Filled Hubbard model and Additional data

In this section, we present additional simulation and experimental data for the problem-agnostic brick circuit qMPS for the doped Fermi-Hubbard chain at 1/3 filling (see Fig. 8).

Noiseless simulations of the problem-agnostic brick-circuit qMPS approach show that it can effectively capture the ground-state and correlations over a range of U and filling-factors.

To minimize the impact of errors, and reduce the implementation time for experimental demonstrations of

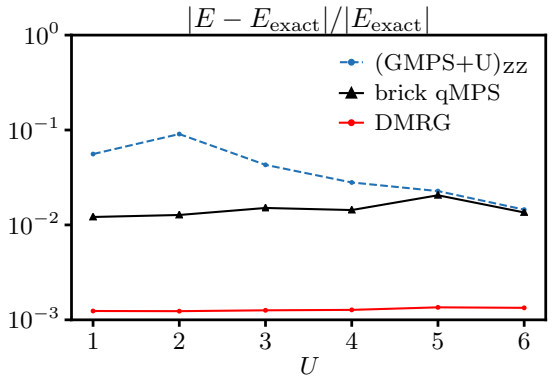

FIG. 8. **Comparing variational results for a 1/3-filled Fermi-Hubbard chain** – (a) relative errors from the exact solutions for the $\frac{1}{3}$-filled Fermi-Hubbard chain of different U's: DMRG solutions with bond dimension 32 (DMRG), simulated results from optimization using the (GMPS+U)zz and VQE methods ($U = 1, 4, 6$ only). The number of variational parameters per site are respectively: 6 ((GMPS + U)zz), 80 (holoVQE), and 1024 (DMRG).)

this brick circuit qMPS, we first classically optimize the circuit-parameters to minimize the variational energy for an infinite MPS (iMPS). From this, we classically compute the steady-state of the bond-transfer matrix, and synthesize a circuit acting on the bond-qubits and one ancilla which approximately prepares this steady-state. This circuit is then used to prepare an initial mixed state of the bond qubits which closely approximates their bulk steady state, allowing us to directly access the infinite system-size limit without iteratively "burning in" the bond-channel as previously done in [7]. We note that a similar technique was employed by [6]. We emphasize that this technique is only viable for small problem sizes where classical simulations are tractable. This, however, may still be useful for preparing, say, a moderate bond-dimension approximation of a correlated ground-state which is subsequently subjected to rapidly-entangling time evolution that could not be simulated classically.

The experimental data agrees well at larger values of U but deviates significantly at $U = 1$. Since the charge correlation length increases with smaller U, we interpret these deviations as arising from increased propagation of noise and errors in large-correlation length qMPS.

In the GMPS+U approach, we also implemented the same simulation for $\frac{1}{3}$-filling states for different U's and the results show similar patterns as the results in half-filling cases.

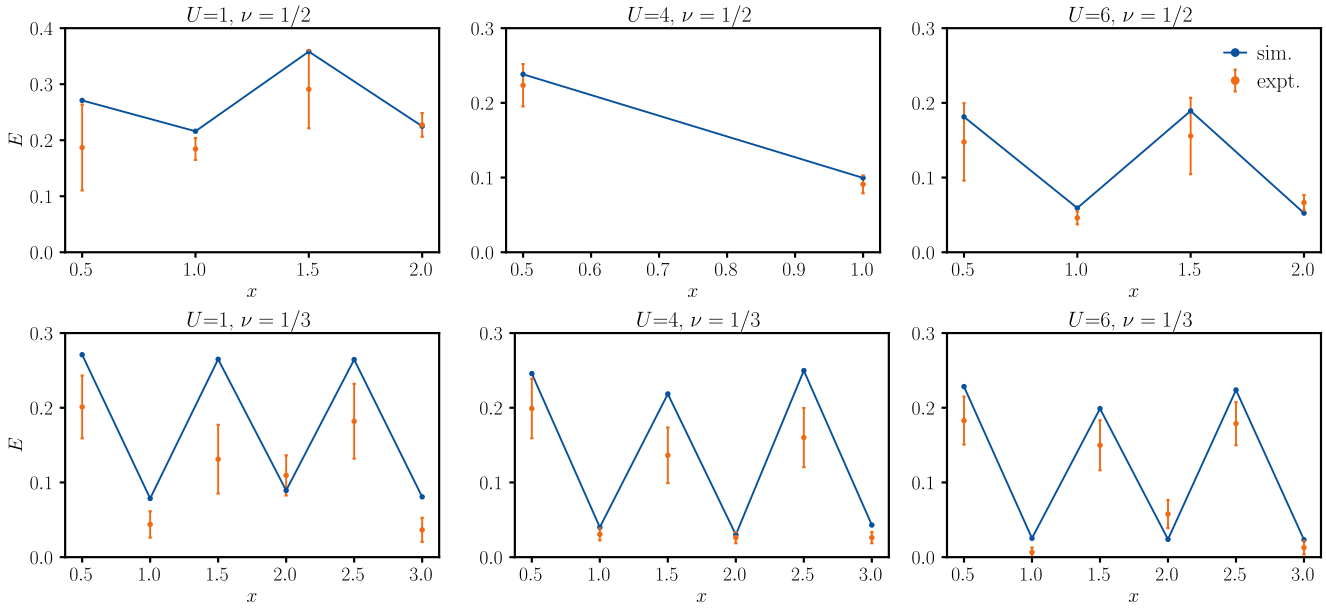

FIG. 9. **brick qMPS method measurement data** of Green's functions and density correlations of the Fermi-Hubbard model of different U's and fillings. Absolute value of hopping energies $t\langle\frac{1}{2}(c^\dagger_{N\uparrow}c_{N+1\uparrow}+c^\dagger_{N\downarrow}c_{N+1\downarrow})\rangle$ are shown at bond-centered coordinates with half-integer positions $x = N - 0.5$, where N labels the spinful sites. On-site repulsion density correlations $\langle n_\uparrow n_\downarrow\rangle$ are shown at site-centered coordinates (integer x).

terms:		$c^\dagger_{\uparrow 0}c_{\uparrow 1}$	$c^\dagger_{\downarrow 0}c_{\downarrow 1}$	$c^\dagger_{\uparrow 1}c_{\uparrow 2}$	$c^\dagger_{\downarrow 1}c_{\downarrow 2}$	$c^\dagger_{\uparrow 2}c_{\uparrow 3}$	$c^\dagger_{\downarrow 2}c_{\downarrow 3}$	$n_{i\uparrow}n_{i\downarrow}$	
U	ν	total shots							success rate
6	1/2	400	400	400	400			1000	58.5%
4	1/2	1000	1000					1000	66.4%
1	1/2	400	400	400	400			1000	42.1%
6	1/3	800	800	800	800	600	800	1000	42.1%
4	1/3	800	800	1000	1000	1000	1000	1000	39.1%
1	1/3	800	1000	800	1200	1000	1000	1000	29.8%

TABLE I. Total shots for different measurements ($i = 1, 2, 3$ for $\frac{1}{3}$-filling states and $i = 1, 2$ for $\frac{1}{2}$-filling states), success rate defines the proportional of total shots kept after the noise mitigation post selection